Research Square

Preprints are preliminary reports that have not undergone peer review.
They should not be considered conclusive, used to inform clinical practice,
or referenced by the media as validated information.

Spatiotemporal Dynamics and Driving Factors of Net Ecosystem Productivity in the Undeveloped Coalfield of Northwestern China: A Case Study of Xinjie Taigemiao

Zhengqiu Yang
National Institute of Clean-and-Low-Carbon Energy
Fang Jie
National Institute of Clean-and-Low-Carbon Energy
Yongqiang Zhao
National Institute of Clean-and-Low-Carbon Energy
Jiawei Guo
20111215@ceic.com

National Institute of Clean-and-Low-Carbon Energy
Suo Zhang
CHN Energy Shenhua Group Xinjie Energy Co., Ltd
Xining Ren
CHN Energy Shenhua Group Xinjie Energy Co., Ltd
Xiaolong Wang
CHN Energy Shendong Coal Group Co., Ltd
Lu Bai
National Institute of Clean-and-Low-Carbon Energy
Wang Zhang
National Institute of Natural Hazards, Ministry of Emergency Management of the People's Republic of China

Article

Keywords: net ecosystem productivity, net primary productivity, land use change, sustainability, coal mining

Posted Date: October 28th, 2026

DOI: https://doi.org/10.21203/rs.3.rs-11150309/v1

License: This work is licensed under a Creative Commons Attribution 4.0 International License.
Read Full License

Additional Declarations: No competing interests reported.

Article type: Original research

Spatiotemporal Dynamics and Driving Factors of Net Ecosystem Productivity in the Undeveloped Coalfield of Northwestern China: A Case Study of Xinjie Taigemiao

Zhengqiu Yang[1], Fang Jie[1], Yongqiang Zhao[1], Jiawei Guo[1*], Suo Zhang[2], Xining Ren[2], Xiaolong Wang[3], Lu Bai[1], Wang Zhang[4]

1. State Key Laboratory of Water Resource Protection and Utilization in Coal Mining, National Institute of Clean-and-Low-Carbon Energy, Beijing 102209, China

2. CHN Energy Shenhua Group Xinjie Energy Co., Ltd., Ordos 017200, China

3. CHN Energy Shendong Coal Group Co., Ltd., Yulin 719315, China

4. National Institute of Natural Hazards, Ministry of Emergency Management of the People's Republic of China, Beijing 100085, China

Corresponding author：Jiawei Guo,20111215@ceic.com

Abstract: Numerous studies have confirmed that coal mining strongly impacts vegetation net ecosystem productivity (NEP). Therefore, evaluating the spatiotemporal dynamics and driving factors of NEP prior to coal mining is crucial for establishing a baseline for ecologically sustainable mining practices. This study utilized the Carnegie-Ames-Stanford Approach (CASA) model combined with empirical models to estimate NEP in the Xinjie Taigemiao Mining Area (XTMA), one of the largest undeveloped coalfields in Northwestern China. We applied slope trend analysis, the Hurst exponent, partial correlation analysis, and geographical detector to evaluate the drivers of NEP. Our findings reveal a distinct spatial pattern in NEP across the XTMA, with higher values observed in the eastern and southern regions and lower values in the western and northern areas. Overall, NEP exhibited a fluctuating yet significant increasing trend during the study period, with 88.7% of the area showing an increase—84.1% of which experienced a gradual rise. The predominant NEP range shifted from 0–100 $gC \cdot m^{-2} \cdot a^{-1}$ to 100–200 $gC \cdot m^{-2} \cdot a^{-1}$. NEP was significantly positively correlated with both temperature and precipitation in most regions. Land use was identified as the most influential driver of NEP, while population density has recently surpassed precipitation as the second most significant factor. These results indicate a continuous improvement in the ecological environment of the XTMA. However, given the potential disturbances from future coal mining, it is imperative to strengthen ecological construction efforts to enhance carbon sequestration capacity and ensure sustainable development.

Key words: net ecosystem productivity; net primary productivity; land use change; sustainability; coal mining

1 Introduction

With the advancement of global industrialization, the continued combustion of fossil fuels and the gradual reduction of forested areas have led to substantial greenhouse gas emissions into the atmosphere, thereby contributing to the increase in the concentration of greenhouse gases[1,2]. Among these gases, carbon dioxide (CO_2) is the dominant contributor, accounting for over 50% of the global warming potential[3,4]. China's CO_2 emissions exceeded 10 billion tons in 2021, with approximately 80% originating from coal consumption[5]. Notably, over 80% of the nation's coal production is sourced from Western China, a trend that continues to grow[6]. This region is predominantly arid and semi-arid, hosting terrestrial ecosystems that are particularly vulnerable to disturbances from both climate change and anthropogenic activities[7–9].

Terrestrial ecosystems constitute a critical component of the global carbon cycle[10,11]. These ecosystems function as a carbon sink when CO_2 absorption by vegetation exceeds carbon release from the surface; otherwise, they act as a carbon source[12]. Therefore, maintaining robust ecosystem health and enhancing vegetation carbon sequestration capacity are fundamental to achieving carbon neutrality goals[13]. In this context, monitoring the carbon sequestration dynamics in the mining areas of Western China has garnered significant research interes[14–16]. Implementing strategies such as intensive mine management[17], sustainability assessment of mining plans[18,19], water consumption restriction, and land reclamation are recognized as vital measures for mitigating the environmental impacts of coal mining[20,21]. Establishing a pre-mining baseline for the spatiotemporal distribution of carbon sequestration capacity is thus crucial for formulating ecologically sustainable mining plans[22].

Net ecosystem productivity (NEP) serves as a key metric for assessing the carbon source-sink dynamics of terrestrial ecosystems[23,24]. Conceptually, NEP represents the net carbon exchange between the ecosystem and the atmosphere, calculated as the difference between net primary productivity (NPP) and heterotrophic respiration (Rh) [25]. The integration of remote sensing-based NPP models with empirical Rh models serves as a pragmatic approach for carbon balance assessment from regional to global scales[26–28], including in coal mining areas. For example, Chen et al. estimated the NEP of an underground coal mining area by using the Miami model and the Rh empirical model[29]. The suitability of three methods—carbon absorption, carbon storage, and net ecosystem productivity—was compared. The results indicate that NEP provides more objective results, although it is relatively complex and requires more extensive data. Yang and Chen[30] employed an improved CASA model to analyze NEP in the Huaibei mining area, confirming its superiority over standard MODIS products. Collectively, studies affirm that mining activities significantly impact vegetation carbon sinks, informing ecological restoration strategies[29–32]. Research on carbon sink capacity in mining areas primarily focuses on ecological restoration and carbon sink enhancement[33,34], the relationship between land use changes and carbon sinks[35–37],

and the construction of carbon sink systems in developed mining areas. There is a lack of relevant research on undeveloped coalfields

The Xinjie Taigemiao Mining Area (XTMA) represents one of the largest undeveloped coalfields in Northwestern China. Its development plan has progressed to the preliminary implementation stage, with the goal of establishing a multi-energy integrated, low-carbon mining area under the ownership of Shenhua Xinjie Energy Co., Ltd. of CHN Energy.

Accurate pre-mining carbon sink data are pivotal for scientifically informing vegetation configuration, land reclamation schemes, and overall sustainable mining practices. To address the identified research gap, this study employs the XTMA as a case study. Specifically, we estimate NEP using an improved CASA model and an empirical Rh model, and analyze the spatiotemporal patterns and driving factors of NEP through partial correlation analysis and geographical detector. The findings aim to provide valuable insights for guiding sustainable coal mining practices in the XTMA.

2 Materials and methods

2.1 Study area

The XTMA is located in the Ordos City, Inner Mongolia Autonomous Region. The area features elevations ranging from 1220 to 1520 meters above sea level, with a general topographic trend sloping from higher northwest to lower southeast (Fig.1). The region is characterized by typical plateau accumulation landforms, extensively covered by Quaternary aeolian deposits, and is classified as semi-desert. The mining area is situated in a temperate continental monsoon climate zone, characterized by significant seasonal variation with rainfall and temperature peaking in the same period. The mean annual temperature is approximately 6.6 °C, with an annual evaporation of 2534.2 mm and an annual precipitation of 434.1 mm. A seasonal river runs through the area, experiencing short-term floods only during the wet season. Ecologically, the mining area lies within the grassland desertification control zone of the Ordos Plateau, an area known for its environmental sensitivity and limited self-restoration capacity[38].

The total planned area of the mining region is approximately 681 km^2, hosting a coal resource reserve of about 1.23 billion tons, rendering it suitable for the development of a modern, large-scale coal base. The planned number of mining fields in the area is eight, with each field having a capacity of no more than 8 Mt/a. The total planned capacity is expected to be 16 Mt/a by 2026 and will reach 56 Mt/a by 2032 [39].

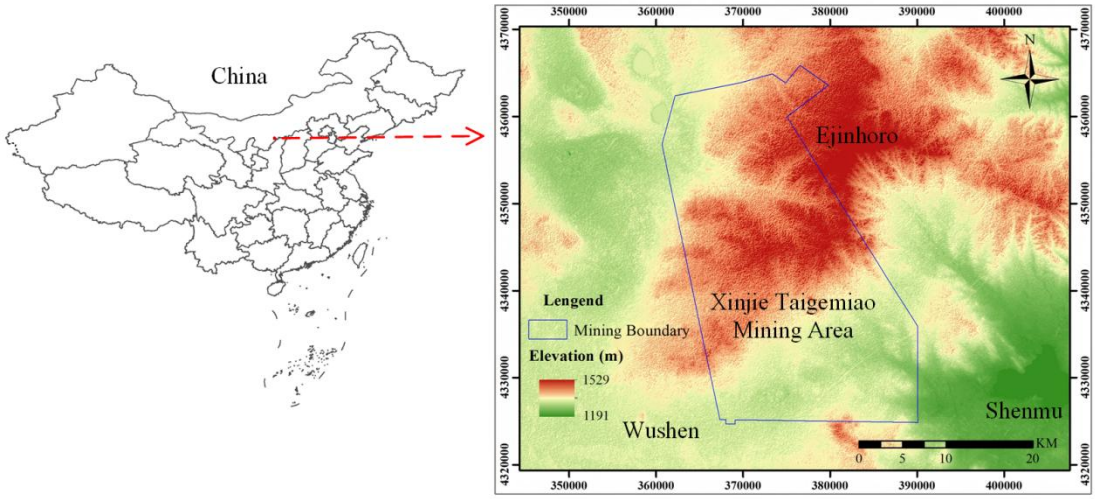


Fig.1 Geographical location and topographic map of the study area

2.2 Data

Landsat series remote sensing data were downloaded from the GEE platform (https://code.earthengine.google.com/) with a spatial resolution of 30 m, and were used to calculate the Ratio Vegetation Index (RVI) and the Simple Vegetation Index (SVI). Temperature and precipitation data were obtained from the website of The National Tibetan Plateau Data Center (http://data.tpdc.ac.cn)[40,41], with a spatial resolution of 1 km. Solar radiation and evapotranspiration data were obtained from the European Centre for Medium-Range Weather Forecasts (https://cds.climate.copernicus.eu), with a spatial resolution of 0.1°. Land use data was sourced from the research of Yang and Huang[42] with a spatial resolution of 30 m. The DEM data were obtained from the ASTER GDEM dataset released on the Geospatial Data Cloud website (https://www.gscloud.cn/), with a spatial resolution of 30 m. The population density data was derived from the LandScan Global dataset released by the Oak Ridge National Laboratory of the U.S. Department of Energy (https://landscan.ornl.gov/), with a spatial resolution of 1 km. The multisource data were preprocessed through projection transformation, resampling, and mask extraction, and the spatial resolution was resampled to 30 m.

2.3 Methods

2.3.1 NPP estimation

The CASA model, a process-based light use efficiency model, estimates NPP as the product of absorbed photosynthetically active radiation (APAR) and the actual light use efficiency (ε) . The core calculation is:

$$NPP(x,t) = APAR(x,t) \times \varepsilon(x,t) \quad (1)$$

NPP represents the net primary productivity of a pixel in a given month ($gC \cdot m^{-2} \cdot month^{-1}$); *APAR* represents the photosynthetically active radiation absorbed by the vegetation of pixel x in month t ($MJ \cdot m^{-2} \cdot month^{-1}$); and $\varepsilon(x,t)$ represents the actual vegetation light use efficiency of pixel x in month t ($gC \cdot MJ^{-1}$).

Light use efficiency is calculated using the temperature stress factor T, the water stress factor W, and the maximum light use efficiency ε_{max}. The calculation formulas are as follow:

$$\varepsilon(x,t) = T_{\varepsilon 1}(x,t) \times T_{\varepsilon 2}(x,t) \times W_{\varepsilon}(x,t) \times \varepsilon_{max} \quad (2)$$

$$T_{\varepsilon 1}(x,t) = 0.8 + 0.02 \times T_{opt}(x) - 0.0005 \times \left[T_{opt}(x)\right]^2 \quad (3)$$

$$(4)\ T_{\varepsilon 2}(x,t) = \frac{1.184}{\left\{1+\exp[0.2\times\left(T_{opt}(x)-10-T(x,t)\right)]\right\}} \times \frac{1}{\left\{1+\exp[0.3\times\left(-T_{opt}(x)-10+T(x,t)\right)]\right\}}$$

$$W_{\varepsilon}(x,t) = 0.5 + 0.5 \times EET_{(x,t)}/PET_{(x,t)} \quad (5)$$

$T_{\varepsilon 1}(x,t)$ and $T_{\varepsilon 2}(x,t)$ represent the first and second temperature stress factors, respectively; $W_{\varepsilon}(x,t)$ represents the water stress factor; ε_{max} represents the maximum light use efficiency of vegetation ($gC \cdot MJ^{-1}$); $T_{opt}(x)$ represents the optimal growth temperature for pixel x during the year (°C); $EET(x,t)$ and $PET(x,t)$ represent the actual evaporation and potential evapotranspiration (mm).

APAR determined by the total solar radiation Q and the vegetation photosynthetically active radiation absorption ratio $FPAR$. The formula is as follows:

$$APAR(x,t) = Q(x,t) \times 0.5 \times FPAR(x,t) \quad (6)$$

$APAR(x,t)$ represents the photosynthetically active radiation absorbed by vegetation in pixel x during t month ($MJ \cdot m^{-2} \cdot month^{-1}$); $Q(x,t)$ represents the total solar radiation ($MJ \cdot m^{-2} \cdot month^{-1}$); and $FPAR(x,t)$ represents the photosynthetically active radiation absorption ratio of vegetation. The formula for calculating $FPAR$ is as follows:

$$FPAR(x,t) = \frac{SEVI - SEVI_{(i,min)}}{SEVI_{(i,max)} - SEVI_{(i,min)}} \times (FPAR_{max} - FPAR_{min}) + FPAR_{min} \quad (7)$$

$$\begin{cases} SEVI(\Delta) = RVI + f(\Delta) \times SVI \\ RVI = \frac{\rho_{NIR}}{\rho_{RED}} \\ SVI = \frac{1}{\rho_{RED}} \\ f_{opt} = argmin(|r1 - r2|), f(\Delta) \in (0.01, 1.000) \\ SEVI = RVI + f_{opt} \times SVI \end{cases} \quad (8)$$

Where $SEVI_{(i,\,min)}$ and $SEVI_{(i,\,max)}$ represent the 5th and 95th percentiles of vegetation cover type i, respectively; $FPAR_{min}$ and $FPAR_{max}$ are 0.001 and 0.95, respectively; ρ_{NIR} and ρ_{RED} represent the reflectance of the near-infrared and red bands, respectively; RVI is the Ratio Vegetation Index; SVI is the Simple Vegetation Index; $f(\Delta)$ is the topographic adjustment factor; The correlation coefficient $r1$ is between $SEVI(\Delta)$ and RVI, and $r2$ is between $SEVI(\Delta)$ and SVI; f_{opt} is the optimal adjustment factor, as the value of $f(\Delta)$ corresponding to the point where $r1$ and $r2$ are closest.

The Synthetic Environmental Vegetation Index (SEVI) constitutes a key improvement of our model over the standard CASA framework. In the standard CASA model, FPAR is typically derived from indices like the Normalized Difference Vegetation Index (NDVI), which are known to be sensitive to soil background brightness and topographic variation, leading to significant uncertainty in semi-arid, undulating landscapes like the XTMA. Our improved SEVI mitigates these limitations through a synthetic approach: by constructing correlation curves between the terrain-adjusted index

$SEVI(\Delta)$ and the two base indices (RVI and SVI), and identifying the optimal adjustment factor f_{opt} where these correlations ($r1$ *and* $r2$) converge most closely. This method dynamically minimizes the combined interference of soil background and terrain, yielding a more robust vegetation signal. The primary advantage of this modification is that it provides a more accurate representation of true vegetation dynamics in our study area compared to using standard indices alone, thereby directly enhancing the reliability of the estimated FPAR, NPP, and the final NEP.

2.3.2 NEP estimation

NEP is an important indicator for assessing the carbon sink capacity of ecosystems. It can be represented as the difference between NPP and soil Rh[24]. In this study, Rh was estimated using an established empirical model that is widely applied in the region[43]. This model posits that Rh is primarily influenced by air temperature and precipitation. The formulas are as follow:

$$NEP = NPP - Rh \tag{9}$$

$$Rh(x,t) = 0.22 \times \left(\exp\left(0.0913T(x,t)\right) + \ln(0.3145P(x,t) + 1)\right) \times 30 \times 46.5\% \tag{10}$$

$Rh(x,t)$ represents the soil respiration of pixel x in the t month ($gC \cdot m^{-2} \cdot month^{-1}$); T represents the average air temperature of pixel x in the t month (°C); and P represents the total precipitation of pixel x in the t month (mm).

The model above was constructed based on long-term national-scale soil respiration observation data. Its form reflects the dominant control of temperature and precipitation on soil respiration. With a simple structure and well-defined parameters, it is suitable for regions like the study area where data are relatively scarce but climate drivers are pronounced. This model was selected for this study due to its robust performance in similar ecoregions and its capacity to accommodate regional heterogeneity.

2.3.3 Slope analysis

To quantify the inter-annual trend of NEP from 2013 to 2022, the slope of the trend was calculated for each pixel using a simple linear regression analysis.. The formula is as follows:

$$S = \frac{n \times \sum_{i=1}^{n}(i \times NEP_i) - \sum_{i=1}^{n} i \times \sum_{i=1}^{n} NEP_i}{n \times \sum_{i=1}^{n} i^2 - (\sum_{i=1}^{n} i)^2} \tag{11}$$

S represents the trend slope of NEP in the mining area; n is the number of years, which is set to 10 in this study; i is the year variable. When S is greater than 0, it indicates an increasing trend in NEP; when S is less than 0, it indicates a decreasing trend in NEP. The absolute value of slope indicates the magnitude of the change.

2.3.4 Hurst exponent

The Hurst exponent (HE) is used to characterize the persistence and memory of a time series [44]. In this study, the R/S analysis method is employed to calculate the HE, which is then used to predict the future trend of NEP in the mining area. The calculation method is as follows:

assuming there is a time series $\{x(t)\}$, $t = 1,2,..,N$, there exists a mean sequence:

$$\bar{x} = \frac{1}{N}\sum_{i=1}^{N} x_i \tag{12}$$

calculate the cumulative deviation sequence $Z(t)$:

$$Z(t) = \sum_{i=1}^{t}(x_i - \bar{x}) \quad (13)$$

the range (R) and standard deviation (S) of the cumulative deviation sequence are defined by the following formulas:

$$R(t) = max(Z(1), Z(2), \dots, Z(t)) - min(Z(1), Z(2), \dots, Z(t)) \quad (14)$$

$$S(t) = \sqrt{\frac{1}{t}\sum_{i=1}^{t}(Z(i) - Z)^2)} \quad (15)$$

the calculation method for the HE is as follows:

$$\log\left(\frac{R(t)}{S(t)}\right) = logC + HE \times \log(t) \quad (16)$$

where C is a constant. When the *HE* is between 0.5 and 1, it indicates that the time series exhibits persistence, with stronger persistence corresponding to higher values. When the *HE* is between 0 and 0.5, it indicates that the time series exhibits anti-persistence, with stronger anti-persistence corresponding to lower values.

2.3.5 Partial correlation analysis

The partial correlation coefficients between NEP and precipitation, temperature, and radiation factors, as well as the p-values for their significance are calculated. By overlaying the partial correlation coefficients and the p-values, the correlation between NEP and each climate driving factor is evaluated. The calculation method for the partial correlation coefficient is as follows:

$$r_{a.bc} = \frac{r_{ab} - r_{ac}r_{bc}}{\sqrt{(1-r_{ac}^2)(1-r_{bc}^2)}} \quad (17)$$

where $r_{a.bc}$ represents the partial correlation coefficient between variables *b* and *c* when controlling for the effect of variable *a*. r_{ab} is the correlation coefficient between variables a and *b*; r_{ac} is the correlation coefficient between variables *a* and *c*; and r_{bc} is the correlation coefficient between variables *b* and *c*.

2.3.6 Geodetector

The Geodetector is a spatial analysis model designed to detect the relationship between independent and dependent variables in spatial data, analyze spatial differentiation of data, and quantify the influence of driving factors[45,46]. It includes four sub-models: factor detector, interaction detector, risk detector, and ecological detector, with results quantified using the q-value. This study utilizes the factor detector and interaction detector to quantify the interaction between different driving factors, assessing whether the joint effects of the independent variables enhance or diminish their explanatory power over the dependent variable. The calculation method is as follows:

$$q = 1 - \frac{\sum_{h=1}^{L} N_h \sigma_h^2}{N\sigma^2} \quad (18)$$

in the formula, *q* represents the differentiation factor, where a larger *q* value indicates more significant differentiation; *L* refers to the categories of the dependent or independent variables; *h* represents a specific category; N_h and σ_h are the number of units and the variance within category *h*, respectively.

Before analyzing with geographic detectors, all continuous drivers (precipitation, temperature, population density, elevation) must be discretized into categorical variables. This study employs the Jenks' natural break method to discretize all climate factors, which maximizes between-group differences while ensuring within-group consistency—a commonly used classification approach in geospatial data analysis. The population density data are discretized according to the official classification standard of LandScan Global, and uniformly divided into 8 levels: 1–5, 6–25, 26–50, 51–100, 101–500, 501–2500, 2501–5000, and >5000 (unit: population·km^{-2}). The classified layers are then used to calculate the q-values for factor detectors and the results for interaction detectors.

3 Results

3.1 Verification of NPP calculation results

The reliability of the estimated NPP and NEP was indirectly evaluated through cross-validation with MODIS NPP products and comparison with published NPP studies in similar regions. Firstly, cross-validation conducted by randomly selecting 100 sample points showed a strong correlation (R^2 = 0.8192) between the calculated NPP and the MODIS NPP product (Fig. 2). Secondly, a comparison with four previous studies (Tab. 1) confirmed that the NPP estimates of this study fall within the reported range for analogous regions and periods, despite differences in specific study areas and timeframes. This consistency supports the reliability of our NPP inversion results..

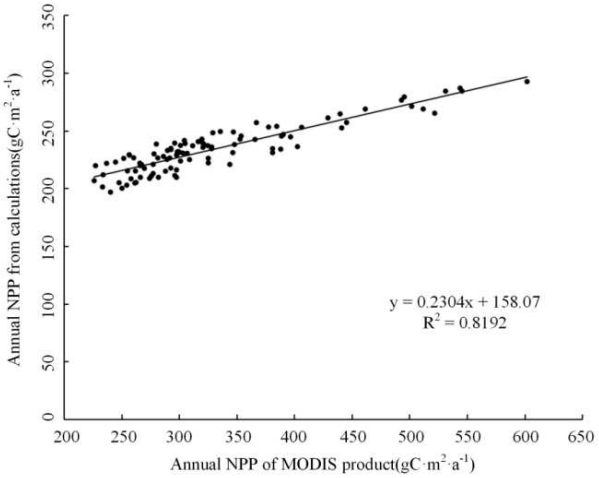


Fig.2 The comparison of the calculated NPP and MODIS NPP in XTMA from 2013 to 2022

Due to the combined effects of climate change, desertification control measures, and the Green for Grain Program, vegetation growth in this region has shown an increasing trend over the past two decades, with a more significant rise after 2010[47]. As a result, the annual NPP exhibits large variations[48], while the multi-year average NPP remains relatively small[49,50]. The NPP estimation of this study is consistent with previous researches.

Tab. 1. The comparison of the calculated NPP values with other research results

Period	Area	Annual NPP (gC·m^{-2}·a^{-1})	Method	Source

2000-2020	Northern Shaanxi	275.12	CASA	Chen et al., 2023
2000-2019	Northern Shaanxi	281.15	MOD17A3HGF	Wei et al., 2022
2006-2020	Pingshuo Mining Area, Northern Shaanxi	342.84–474.48	CASA	Fu et al., 2022
2001-2020	the Loess Plateau, Northern Shaanxi	240.7–422.5	CASA	Mao et al., 2024
2013-2022	XTMA, Northern Shaanxi	274–336	CASA	Our study

3.2 The Spatiotemporal evolution characteristics of NEP

3.2.1 Spatial distribution characteristics of NEP

The spatial distribution of NEP across the XTMA from 2013 to 2022 is presented in Fig. 3(a-e). It can be seen that the distribution characteristics of NEP in the XTMA are higher in the east and lower in the west, with the south being higher than the north, overall showing a carbon sink. The multi-year average NEP value is 127.10 $gC \cdot m^{-2} \cdot a^{-1}$. The maximum value of NEP is 506.10 $gC \cdot m^{-2} \cdot a^{-1}$ and the minimum value is -183.08 $gC \cdot m^{-2} \cdot a^{-1}$.

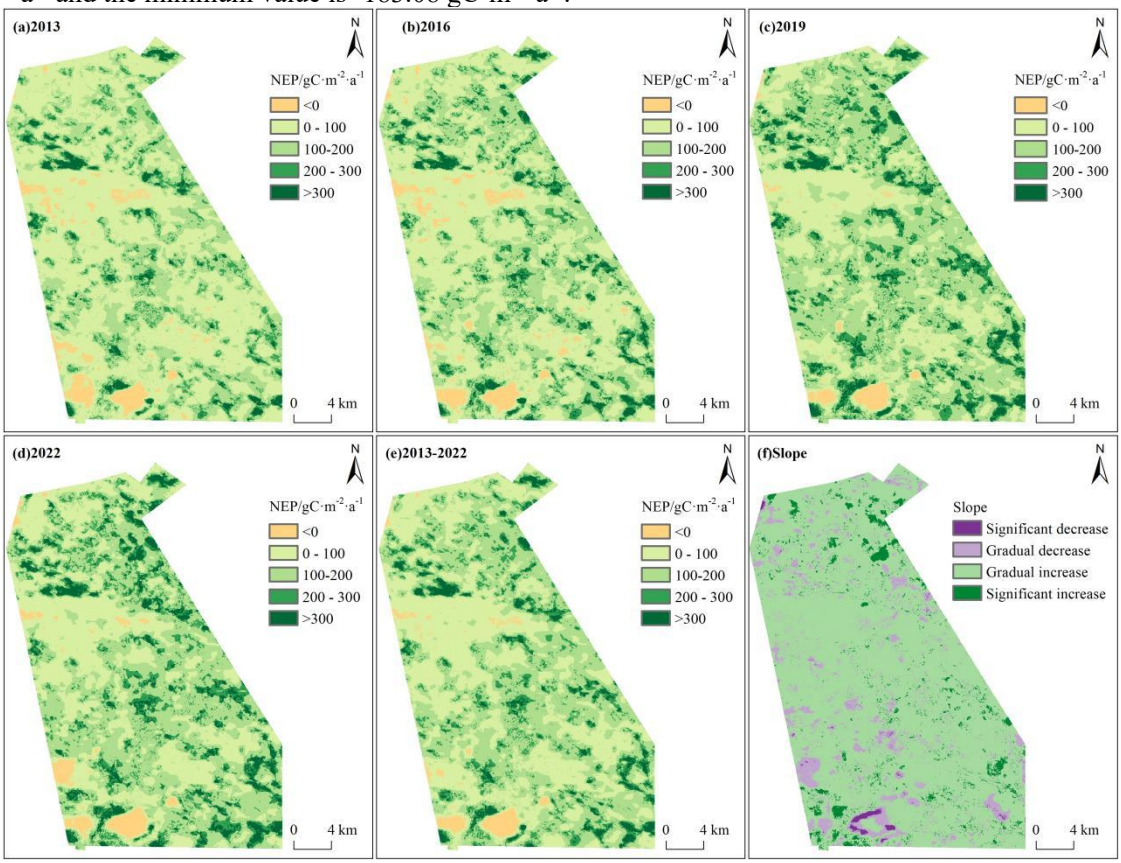


Fig.3 (**a, b, c, d**) NEP in 2013, 2016, 2019 and 2022, respectively; (**e**) multi-year average NEP from 2013 to 2022; and (**f**) the slope of NEP in the XTMA

In terms of NEP magnitude classes, the 100–200 $gC \cdot m^{-2} \cdot a^{-1}$ range accounted for the largest proportion (43.8%) of the area and was widely distributed (Fig. 3e). This was followed by the 0–100 $gC \cdot m^{-2} \cdot a^{-1}$ (38.1%), primarily located in the central-western and southern XTMA. Areas with the strongest carbon sink capacity (NEP>300 $gC \cdot m^{-2} \cdot a^{-1}$) only occupy a proportion of 4.4%. Meanwhile, the carbon source area, with NEP<0 $gC \cdot m^{-2} \cdot a^{-1}$, has the lowest proportion (2.3%) and

is mainly distributed in the southwest corner and a small area in the western part of the northern region of the XTMA.

3.2.2 Inter-annual variation of NEP

Fig. 4 illustrates a significant fluctuating upward trend in the annual average NEP across the XTMA, increasing from a minimum of 89.81 $gC \cdot m^{-2} \cdot a^{-1}$ in 2015, and the maximum annual average NEP value was 146.49 $gC \cdot m^{-2} \cdot a^{-1}$ in 2021. As shown in Tab. 2, the interval with the highest proportion of NEP over the ten years gradually shifted from 0–100 $gC \cdot m^{-2} \cdot a^{-1}$ to 100–200 $gC \cdot m^{-2} \cdot a^{-1}$. The proportion of NEP less than 0 $gC \cdot m^{-2} \cdot a^{-1}$ showed little change and remained at a low level. The proportion of annual average NEP in the 0–100 $gC \cdot m^{-2} \cdot a^{-1}$ range exhibited a fluctuating decreasing trend. The proportion of NEP in the 100–200 $gC \cdot m^{-2} \cdot a^{-1}$ range showed a fluctuating increasing trend and remained at a relatively high level. The proportion of annual average NEP in the 200–300 $gC \cdot m^{-2} \cdot a^{-1}$ and greater than 300 $gC \cdot m^{-2} \cdot a^{-1}$ ranges exhibited a clear increasing trend, maintaining a high level during 2021–2022.

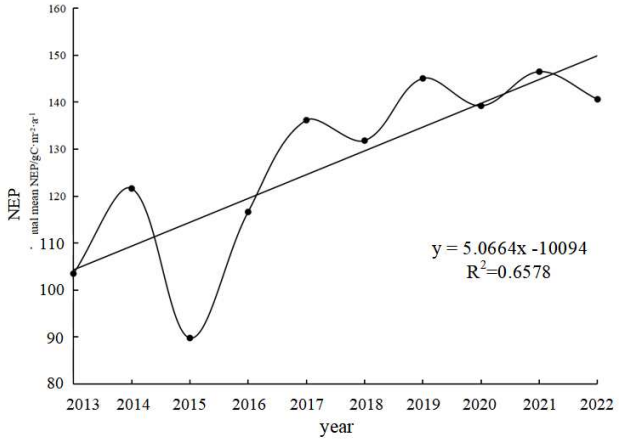


Fig.4 Scatter plot of the annual average NEP of the XTMA from 2013 to 2022

Tab.2 Proportion of NEP at all levels in the XTMA from 2013 to 2022

Year	The area proportion of NEP at different levels (%)				
	NEP<0	0<NEP<100	100<NEP<200	200<NEP<300	NEP>300
2013	3.7	53.1	31.6	8.7	2.9
2014	2.5	43.0	38.9	10.8	4.8
2015	4.5	60.9	26.0	7.0	1.6
2016	3.8	44.3	37.1	10.2	4.5
2017	2.5	34.5	43.7	12.8	6.5
2018	2.6	35.8	43.7	12.2	5.7
2019	1.8	28.1	49.7	13.7	6.7
2020	1.9	31.3	47.9	12.7	6.2
2021	2.5	28.0	47.7	14.5	7.4
2022	2.9	31.4	44.6	14.0	7.2

3.2.3 NEP Trend Analysis

The calculated Slope values for NEP across the XTMA ranged from -71.5 to 54.1, with a mean value of 4.8 (Fig.3f). This indicates a predominant increasing trend in NEP, observed in 88.7% of the total area. Of this increasing area, the majority (84.1% of the total area) exhibited a gradual

increase, widely distributed across the region, while a smaller portion (4.6%) showed a significant increase, concentrated in the northern and southern sectors. Areas exhibiting a decreasing trend in NEP accounted for 11.3% of the XTMA, with gradual decreases (10.7%) being scattered and significant decreases (0.6%) primarily located in the south..

From 2013 to 2022, the HE of XTMA ranged from 0.17 to 0.70, with an average value of 0.58 (Fig.5a). This result indicates a strong persistence in the temporal dynamics of NEP across most of the study area, as 86.3% of the region exhibited an HE greater than 0.5. In contrast, anti-persistent behavior was relatively uncommon, characterizing only 13.7% of the area, with a notably higher concentration observed in the northern sectors. The spatial projection of future NEP trends, derived from the HE, identified four distinct categories (Fig.5b). The landscape is overwhelmingly dominated by a persistent increase, encompassing 78.3% of the total area, primarily located in the central and southern parts. Conversely, a persistent decrease is projected for 8.0% of the region, mainly distributed in the southwestern part. The areas of anti-persistent increase and anti-persistent decrease account for 10.4% and 3.3%, respectively, with no obvious pattern in their distribution.

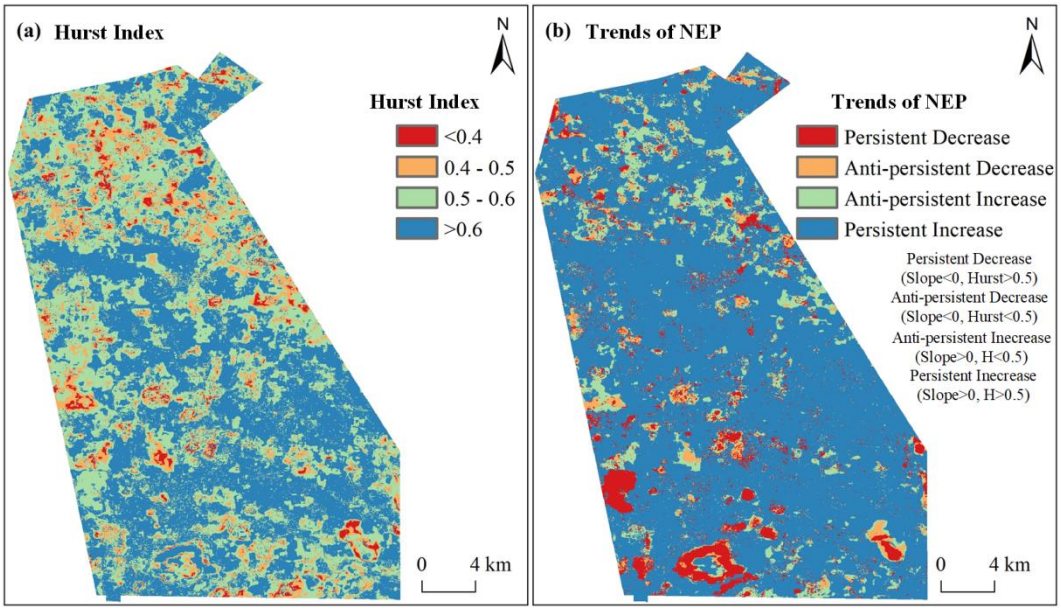


Fig.5 Spatial distribution of the Hurst exponent and projected future trends of NEP in the XTMA from 2013 to 2022

3.3 Analysis of NEP driving factors

3.3.1 Partial correlation analysis between climate factors and NEP

This study employed partial correlation analysis to examine the three main climate drivers affecting NEP: precipitation, temperature, and radiation. The correlation was classified into six levels: highly significant negative correlation (HSNC, $r<0$, $P\leq0.01$), significant negative correlation (SNC, $r<0$, $0.01<P\leq0.05$), non-significant negative correlation (NSNC, $r<0$, $P>0.05$), non-significant positive correlation (NSPC, $r>0$, $P>0.05$), significant positive correlation (SPC, $r>0$, $0.01<P\leq0.05$), and highly significant positive correlation (HSPC, $r>0$, $P\leq0.01$).

Partial correlation analysis reveals distinct response patterns of NEP to climatic drivers across the XTMA (Fig.6). Statistically, NEP demonstrated a significant positive correlation with both

temperature and precipitation, with mean partial correlation coefficients of 0.37 and 0.26, respectively, indicating a stronger climatic association with temperature. Spatially, this relationship is evident in the vast majority of the region, where 93.0% of the area exhibits a positive correlation with temperature and 90.9% with precipitation. Conversely, NEP is predominantly negatively correlated with solar radiation, characterized by a strong mean partial correlation coefficient of -0.99. This negative association is spatially extensive, affecting 64.2% of the mining area, with the most pronounced negative correlations clustered in the southwestern sector.

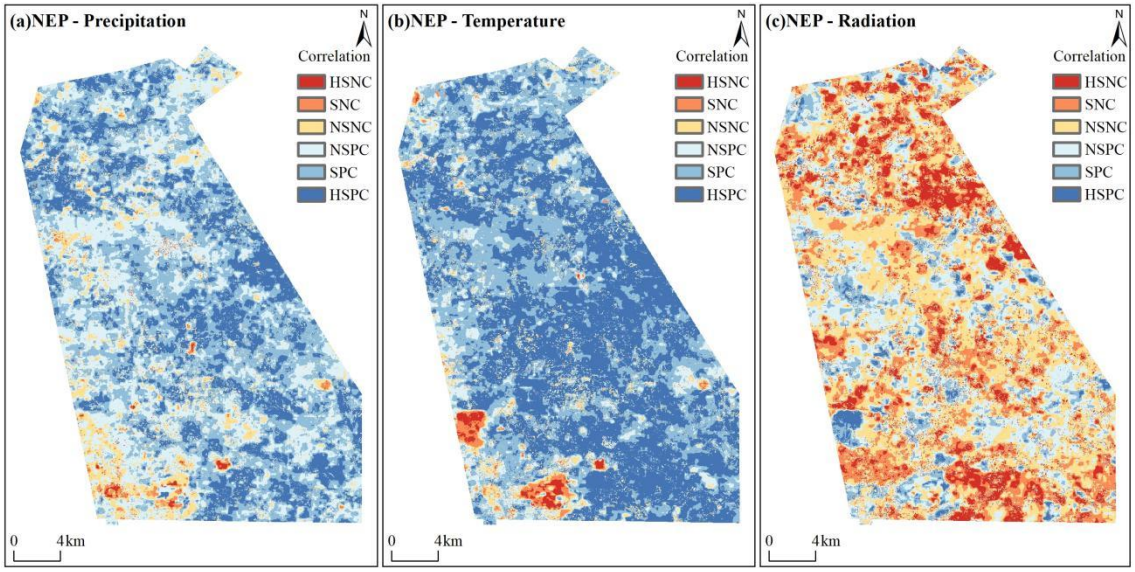


Fig.6 Correlation between NEP and precipitation, temperature and radiation in mining area from 2013 to 2022

3.3.2 Land use change

The land use types in the mining area (Fig.7) are predominantly grassland, followed by cropland, with the respective areas being 630.74 km^2 and 147.16 km^2 in 2022. Impervious surfaces are primarily located in the southwestern part of the mining area. Over the past decade, the distribution of land use types has remained stable, while the total area of cropland and grassland has experienced significant fluctuations. The cropland area increased by 16.46 km^2, whereas the grassland area decreased by 19.43 $km^{2.}$ The average NEP of grassland and cropland also show an increasing trend, they are the main land use types contributing to NEP in the XTMA. As shown in Tab. 3, the average NEP of arable land, forests, and grasslands showed varying degrees of increase from 2013 to 2022. The carbon sink capacity of grassland saw the greatest increase (41.2%), followed by forestland (23.6%), and cropland showing the smallest increase (18.9%).

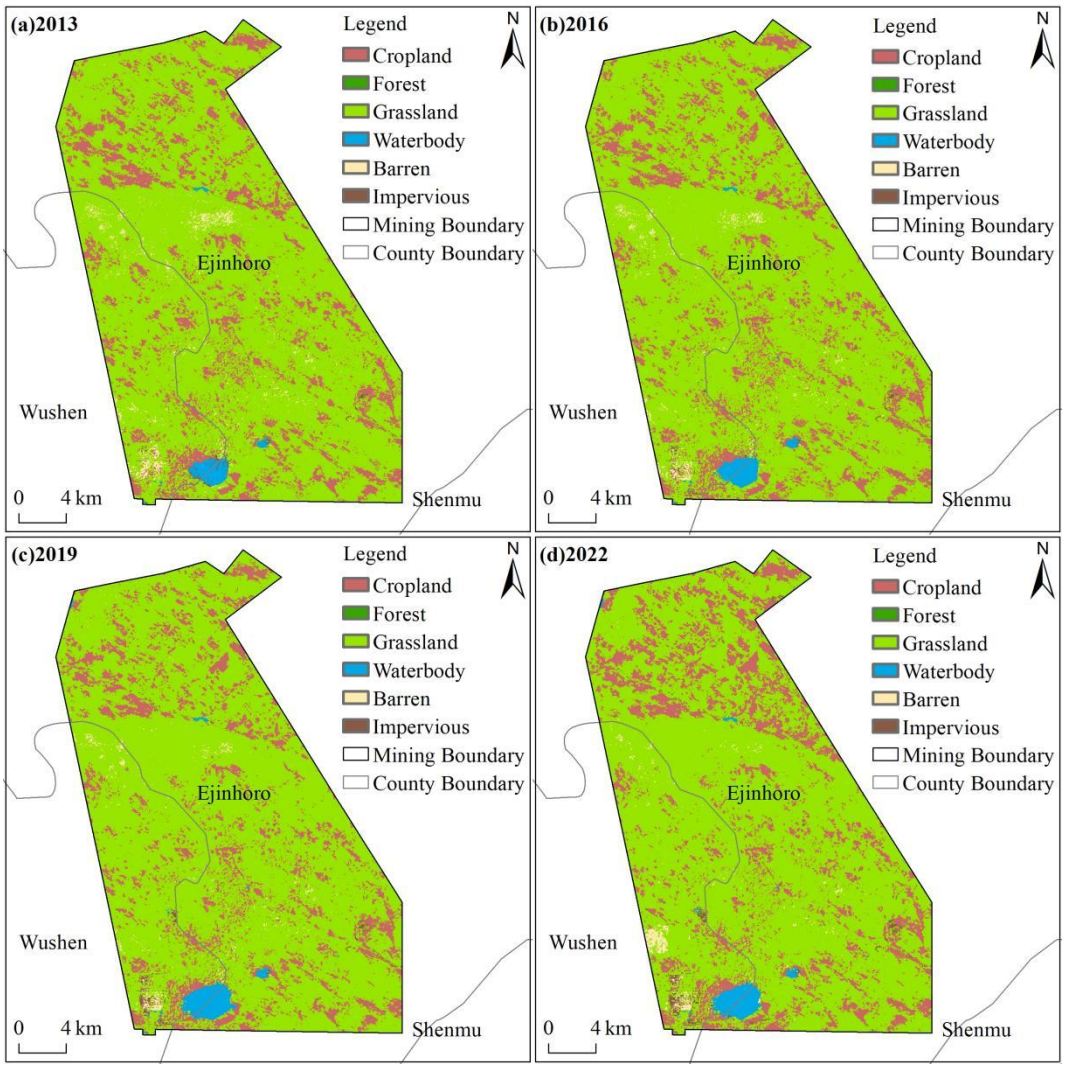


Fig.7 Land use type distribution map of mining area in 2013, 2016 and 2022

Tab.3 NEP and area changes of different land use types in XTMA from 2013 to 2022

Land use type	Average NEP($gC \cdot m^{-2} \cdot a^{-1}$)		Changes in area (km^2)	Changes in net ecosystem carbon accumulation (tC)
	2013	2022		
Cropland	232.66	276.60	16.46	10295.90
Forest	196.71	243.22	0.99	242.85
Grassland	80.77	114.04	-19.43	19416.09
Water body	-111.60	-108.35	4.10	-423.75
Barren	44.49	24.34	-4.32	-321.21
Impervious	60.32	133.45	2.21	503.87

3.3.3 Geo-detector analysis results

The results from the Geodetector analysis, based on the mean q-values from 2013 to 2022 (Fig. 8), ranked the explanatory power of the driving factors on NEP as follows: land use (0.24) > precipitation (0.15) > population density (0.13) > temperature (0.03) > elevation (0.01). This

hierarchy indicates that anthropogenic factors, particularly land use, were the dominant drivers of NEP variation in the XTMA. Among the climatic factors, precipitation exerted a stronger influence than temperature. And the factors with the highest explanatory power for NEP from 2021 to 2022 were land use and population density, followed by precipitation and land use.

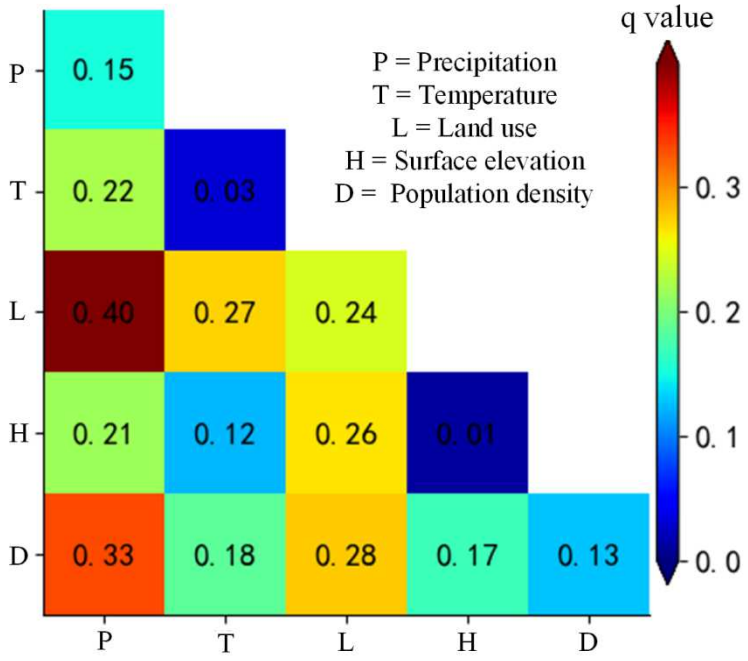


Fig.8 The single-factor influence and interaction q-values of the NEP mean values

Tab.4 Top three interactive factors explaining NEP variations during different periods

Period	Rank 1 interaction (q)	Rank 2 interaction (q)	Rank 3 interaction (q)
2013–2014	Precipitation ∩ Land use (0.32)	Precipitation ∩ Population density (0.28)	Precipitation ∩ Elevation (0.25)
2015–2016	Precipitation ∩ Land use (0.37)	Precipitation ∩ Population density (0.33)	Precipitation ∩ Temperature (0.29)
2017–2018	Precipitation ∩ Land use (0.42)	Precipitation ∩ Population density (0.35)	Land use ∩ Population density (0.32)
2019–2020	Precipitation ∩ Land use (0.37)	Precipitation ∩ Population density (0.33)	Land use ∩ Population density (0.29)
2021–2022	Land use ∩ Population density (0.38)	Precipitation ∩ Land use (0.37)	Temperature ∩ Land use (0.33)

The q-values of all two-factor interactions were consistently higher than those of the corresponding single factors, indicating a pronounced nonlinear enhancement effect (Tab.4). Analysis of interaction effects across five representative time periods revealed that, from 2013 to 2020, the combination of precipitation and land use exhibited the strongest explanatory power for NEP, with q-values of 0.32, 0.37, 0.42, and 0.37, respectively. During the same period, the interaction between precipitation and population density ranked as the second most influential factor. In contrast, from 2021 to 2022, the interaction between land use and population density became the dominant driver of NEP variation, followed by the interaction between precipitation and land use.

4 Discussion

4.1 The carbon sink changes in the XTMA

The spatiotemporal evolution characteristics of carbon sinks in the XTMA demonstrate a distinct fluctuating yet upward trajectory in annual average NEP, with persistence analysis indicating a high probability of continued growth, confirming the region's role as a net carbon sink. This finding aligns with broader regional trends observed in other mining areas. For instance, Dai[51] and Ke[52] documented similar fluctuating increases in Net Primary Productivity (NPP) in the Shendong mining area over the past two decades. While these studies corroborate the historical trend, our research extends this understanding by quantitativelyy projecting a persistent future increase, a dimension not previously explored.

Spatially, the NEP exhibits a pattern of higher values in the eastern and southern parts of the mining area and lower values in the western and northern regions. This "high in southeast, low in northwest" spatial heterogeneity arises from the combined effects of natural predispositions and human activities. From the perspective of natural baseline conditions, the overall terrain of the study area slopes from higher northwest to lower southeast (Fig.1). The relatively lower elevation and gentler topography in the southeast may be more conducive to soil moisture retention and vegetation growth, forming a foundational natural advantage. The SEVI index employed in our improved CASA model partially corrects for topographic effects, aiming to more accurately extract the vegetation signal. Crucially, the distribution of land use types serves as the key proximate driver explaining this spatial pattern (Fig.7). The southeastern areas concentrate more cropland and grassland with higher coverage, ecosystems that typically possess greater carbon sequestration capacity. In contrast, the vegetation cover in the northwestern grasslands is relatively sparse, interspersed with patches of barren land, leading to a lower average NEP. Furthermore, the localized areas of low NEP or even carbon sources (NEP < 0) observed in the southwest (Fig. 3a – e) show a high degree of overlap with the distribution of construction land (impervious surfaces, Fig.7), providing direct evidence of the suppressive effect of intense anthropogenic disturbance on carbon sink functionality. Specifically, as illustrated in Fig.s 3f and 5b, the northeastern part is projected to experience a predominant increase in NEP. In contrast, certain southwestern areas are expected to see a persistent decrease. This decline is largely attributable to land use changes, where original grasslands and croplands have been converted to impermeable surfaces, water bodies, and bare land for urban development. This transformation disrupts the native ecosystem and consequently diminishes the region's carbon sequestration capacity. Furthermore, ongoing development and construction are likely to increase population density, making this land conversion a continuing trend. It is important to note that the time series length (N=10 years, 2013-2022) used for the R/S analysis to calculate the Hurst exponent may impose constraints on the statistical robustness of the derived persistence measure. Nevertheless, longer future observational records will undoubtedly enhance the reliability of the persistence prediction. Validating and potentially refining the projections presented here as the time series extends will be an important direction for future

research.

4.2 Climate and anthropogenic drivers of carbon sink in the XTMA

The significant improvement in the vegetation ecology and carbon sink capacity in northern China over the past decade is widely documented[53,54], a phenomenon largely attributed to regional climate shifts, including the northward migration of the precipitation belt and rising temperatures. Our findings corroborate that temperature and precipitation are key climatic drivers of NEP in the XTMA, with 93.0% and 90.9% of the area showing positive correlations, respectively. However, the geographical detector analysis reveals a more nuanced hierarchy: precipitation (q=0.15) exerts a significantly stronger influence than temperature (q=0.03), establishing it as the dominant climatic factor. This aligns with studies in similar arid and semi-arid environments[55] and is ecologically coherent for the XTMA, located on the fringe of the Mu Us Desert where water availability is the primary limiting factor for plant growth and photosynthesis[56].The role of temperature is more complex and potentially dualistic. Given the region's relatively low annual average temperature (7.46-8.05C), a moderate increase could potentially enhance soil temperature, accelerate the mineralization of soil organic matter, and thus benefit NEP. Conversely, sustained warming may also intensify soil respiration rates and exacerbate water stress through elevated evapotranspiration, ultimately suppressing NPP and leading to a reduction in NEP[16]. Additionally, NEP showed a significant negative correlation with solar radiation (mean partial correlation coefficient of -0.99). This has a plausible ecological explanation in arid and semi-arid regions: intense solar radiation increases surface evapotranspiration, leading to rapid soil moisture loss and consequently intensified vegetation water stress. In a precipitation-limited region like the XTMA, water is the primary constraint on plant growth. Therefore, high radiation levels are often associated with more severe water stress, which inhibits photosynthesis and leads to lower NEP. This further underscores the importance of precipitation as the dominant climatic factor in the study area.

Anthropogenic drivers, however, demonstrate an even more profound influence. Analysis of the land use transition matrix (Tab.5) highlights dynamic conversions, most notably from grassland to cropland (8.4%) and from cropland to grassland (27.5%), changes largely driven by ecological restoration programs like the "Three-North Shelter Forest Program" and the "Grain for Green Initiative". The geographical detector identifies land use change as the single most powerful driver of NEP (q = 0.24), a finding consistent with nearby major coal mining regions[14,30]. Notably, population density has recently surpassed precipitation to become the second most influential factor. The geographical detector analysis indicates that population density has become the second most important driver, second only to land use. This is likely because areas with concentrated populations are often associated with more intensive land use changes (e.g., expansion of construction land), more frequent human activity disturbances (e.g., grazing, transportation), and potential indirect pressures on surrounding vegetation (e.g., changes in groundwater levels, pollution dispersion). The significant non-linear enhancement effect observed from the interaction between land use and population density (Tab.4) further confirms that the spatial agglomeration of human activities is a

key process altering surface cover and thereby affecting the carbon sink function of ecosystems. The significant non-linear enhancement effect observed from the interaction between land use and population density underscores that concentrated human activities, which catalyze both land conversion and population aggregation, are primary disruptors of the ecological environment and key constraints on ecosystem carbon sink capacity.

Tab.5 Land use transition matrix of the XTMA between 2013 and 2022.

Land use type		2022					
		Cropland	**Forest**	**Grassland**	**Water body**	**Barren**	**Impervious**
2013	Cropland	92.09	0.74	35.95	1.15	0.13	0.64
	Forest	0.01	0.03	0.01	0.00	0.00	0.00
	Grassland	54.64	0.27	586.35	1.97	4.13	2.81
	Water body	0.04	0.00	0.06	6.13	0.00	0.03
	Barren	0.15	0.00	7.88	0.11	2.11	0.47
	Impervious	0.23	0.00	0.48	0.99	0.03	1.13

In conclusion, the future of carbon sinks in the XTMA will be shaped by the interplay of climate change and intensifying human activities[25]. In the context of global warming, a decline in the recent relatively abundant precipitation would exacerbate drought stress on vegetation, thereby suppressing its carbon sequestration capacity. Therefore, although the vegetation in the northern semi-arid regions of China is showing an overall positive trend, we need to strengthen ecological protection measures during mining area development to cope with the uncertainties brought about by future climate change.

5 Conclusion

This study quantified the NPP and NEP in the XTMA from 2013 to 2022 utilizing an improved CASA model and an empirical respiration model. The spatiotemporal dynamics and future persistence of NEP were examined through trend analysis and the Hurst exponent, while the underlying drivers were investigated using partial correlation analysis and the geographical detector method. The main conclusions are as follows:

(1) The XTMA ecosystem functioned as a net carbon sink, with significant spatial heterogeneity in NEP. The multi-year average NEP was 127.10 $gC \cdot m^{-2} \cdot a^{-1}$. Spatially, NEP exhibited a distinct pattern of being higher in the eastern and southern regions and lower in the western and northern areas. The dominant NEP range shifted from 0-100 $gC \cdot m^{-2} \cdot a^{-1}$ to 100-200 $gC \cdot m^{-2} \cdot a^{-1}$, which accounted for 43.8% of the total area, indicating an overall enhancement of the regional carbon sink capacity during the study period.

(2) Interannual NEP dynamics showed a fluctuating yet significantly increasing trend, with a high probability of persistence. The lowest annual average NEP value (89.81 $gC \cdot m^{-2} \cdot a^{-1}$) was recorded in 2015, while the peak value (146.49 $gC \cdot m^{-2} \cdot a^{-1}$) occurred in 2021. Trend analysis

revealed that 88.7% of the area exhibited an increasing NEP trend. More importantly, analysis based on the Hurst exponent indicated that in 86.3% of the XTMA, the NEP change trend shows continuity, with 78.3% of the area exhibiting a sustained increase.

(3) NEP dynamics result from both climatic and anthropogenic factors, with human influence becoming increasingly dominant. Partial correlation analysis shows significant positive correlations between NEP and temperature (93.0% of the area) and precipitation (90.9% of the area), where precipitation acts as the primary climatic driver ($q = 0.15$). However, geographical detector analysis identifies land use change ($q = 0.24$) as the strongest factor explaining NEP spatial variation. Notably, population density ($q = 0.13$) has recently surpassed precipitation as the second most important driver. Interaction detector results further show that land conversion and population aggregation dominate in regulating regional carbon sink capacity.

This study provides a crucial ecological baseline for future coal mining activities in the XTMA. The findings emphasize that throughout the impending large-scale mining development, it is imperative to implement stringent ecological protection measures, optimize land use planning, and enhance vegetation restoration and management. These actions are essential to mitigate potential ecological disturbances from mining, maintain and enhance the regional carbon sequestration capacity.

Research funding

This research did not receive funding.

Data availability

The datasets used and/or analysed during the current study available from the corresponding author on reasonable request.

Ethics statement

All authors have read, understood, and have complied as applicable with the statement on "Ethical responsibilities of Authors" as found in the Instructions for Authors

References

1. Long, X., Naminse, E. Y., Du, J. & Zhuang, J. Nonrenewable energy, renewable energy, carbon dioxide emissions and economic growth in China from 1952 to 2012. *Renewable & Sustainability Energy Reviews* **52**, 680–688 (2015).
2. Woodwell, G. M. The warming of the industrialized middle latitudes 1985–2050: Causes and consequences. *Climatic Change* **15**, 31–50 (1989).
3. IPCC. *Climate Change 2021: The Physical Science Basis. Contribution of Working Group I to the Sixth Assessment Report of the Intergovernmental Panel on Climate Change*. (Cambridge University Press, Cambridge, United Kingdom and New York, NY, USA, 2021). doi:10.1017/9781009157896.
4. Bera, D. *et al.* Assessment of Carbon Stock and Sequestration Dynamics in Response to Land Use and Land Cover Changes in a Tropical Landscape. *Land* **13**, 1689 (2024).
5. *BP Statistical Review of World Energy 2022*. (2022).
6. Zhang, Y. *et al.* Remarkable Spatial Disparity of Life Cycle Inventory for Coal Production in China. *Environmental Science & Technology* **57**, 15443–15453 (2023).
7. Guan, D., Hubacek, K., Weber, C. L., Peters, G. P. & Reiner, D. M. The drivers of Chinese CO2 emissions from 1980 to 2030. *Global Environmental Change* **18**, 626–634 (2008).
8. Heimann, M. & Reichstein, M. Terrestrial ecosystem carbon dynamics and climate feedbacks. *Nature* **451**, 289–292 (2008).
9. Lu, Z. *et al.* Soil moisture seasonality alters vegetation response to drought in the Mongolian Plateau. *Environmental Research Letters* **16**, 014050 (2021).
10. Poulter, B. *et al.* Contribution of semi-arid ecosystems to interannual variability of the global carbon cycle. *Nature* **509**, 600–603 (2014).
11. Christensen, L., Coughenour, M. B., Ellis, J. E. & Chen, Z. Z. Vulnerability of the Asian Typical Steppe to Grazing and Climate Change. *Climatic Change* **63**, 351–368 (2004).
12. Zhou, W., Huang, L., Yang, H., Ju, W. & Yue, T. Interannual variation in grassland net ecosystem productivity and its coupling relation to climatic factors in China. *Environmental Geochemistry and Health* **41**, 1583–1597 (2019).
13. Fatichi, S., Pappas, C., Zscheischler, J. & Leuzinger, S. Modelling carbon sources and sinks in terrestrial vegetation. *New Phytologist* **221**, 652–668 (2019).
14. Huang, Y., Tian, F., Wang, Y., Wang, M. & Hu, Z. Effect of coal mining on vegetation disturbance and associated carbon loss. *Environmental Earth Sciences* **73**, 2329–2342 (2015).
15. Dai, L. *et al.* Multi Scale Evaluation of the Impact of High-Intensity Mining on Vegetation Carbon Sequestration Capacity. *Sustainability* **16**, 10208 (2024).
16. Yang, B. *et al.* Dynamic Changes in Carbon Sequestration from Opencast Mining Activities and Land Reclamation in China's Loess Plateau. *Sustainability* **11**, 1473 (2019).

17. Guo, P., Qi, X., Zhou, X. & Li, W. Total-factor energy efficiency of coal consumption: An empirical analysis of China's energy intensive industries. *Journal of Cleaner Production* **172**, 2618–2624 (2018).
18. Ma, Q., Wu, J., He, C. & Fang, X. The speed, scale, and environmental and economic impacts of surface coal mining in the Mongolian Plateau. *Resources, Conservation and Recycling* **173**, 105730 (2021).
19. Mohsin, M., Zhu, Q., Naseem, S., Sarfraz, M. & Ivascu, L. Mining Industry Impact on Environmental Sustainability, Economic Growth, Social Interaction, and Public Health: An Application of Semi-Quantitative Mathematical Approach. *Processes* **9**, 972 (2021).
20. Xu, W., Wang, J., Zhang, M. & Li, S. Construction of landscape ecological network based on landscape ecological risk assessment in a large-scale opencast coal mine area. *Journal of Cleaner Production* **286**, 125523 (2021).
21. Feng, Y., Wang, J., Bai, Z. & Reading, L. Effects of surface coal mining and land reclamation on soil properties: A review. *Earth-Science Reviews* **191**, 12–25 (2019).
22. Yang, B., Bai, Z., Fu, S. & Cao, Y. Division of carbon sink functional areas and path to carbon neutrality in coal mines. *International Journal of Coal Science & Technology* **9**, 48 (2022).
23. Huang, Y. *et al.* Changes and net ecosystem productivity of terrestrial ecosystems and their influencing factors in China from 2000 to 2019. *Frontiers in Plant Science* **14**, 1120064 (2023).
24. Zhang, J., Hao, X. M., Hao, H., Fan, X. & Li, Y. Climate change decreased net ecosystem productivity in the Arid Region of central Asia. *Remote Sensing* **13**, 4449 (2021).
25. Yang, Y., Gong, R., Liu, S., Wu, Q. & Chen, F. The Loss and Recovery Potential of Net Ecosystem Productivity in Mining Areas: A Global Assessment Based on Data for 2000–2020. *Land* **13**, 1913 (2024).
26. Mitchard, E. T. A. The tropical forest carbon cycle and climate change. *Nature* **559**, 527–534 (2018).
27. Hashimoto, S. *et al.* Global spatiotemporal distribution of soil respiration modeled using a global database. *Biogeosciences* **12**, 4121–4132 (2015).
28. Piao, S. *et al.* Net carbon dioxide losses of northern ecosystems in response to autumn warming. *Nature* **451**, 49–52 (2008).
29. Chen, F. *et al*. Assessing carbon sink capacity in coal mining areas: a case study from Taiyuan City, China. *Atmosphere* **15**, 765 (2024).
30. Yang, H. & Chen, W. Spatio-temporal pattern of urban vegetation carbon sink and driving mechanisms of human activities in Huaibei, China. *Environmental Science and Pollution Research* **29**, 31957–31971 (2022).
31. Mylliemngap, W. & Barik, S. K. Plant diversity, net primary productivity and soil nutrient

contents of a humid subtropical grassland remained low even after 50 years of post-disturbance recovery from coal mining. *Environmental Monitoring and Assessment* **191**, 697 (2020).

32. Chen, Z. *et al.* Study on spatio-temporal evolution of ecosystem services, spatio-temporal pattern of tradeoff/synergy relationship and its driving factors in Shendong mining area. *Frontiers in Environmental Science* **12**, (2024).
33. Zhu, X. *et al.* Assessing the impacts of ecological governance on carbon storage in an urban coal mining subsidence area. *Ecological Informatics* **72**, 101901 (2022).
34. Liao, Q., Liu, X. & Xiao, M. Ecological restoration and carbon sequestration regulation of mining Areas—a case study of Huangshi City. *International Journal of Environmental Research and Public Health* **19**, 4175 (2022).
35. Qiu, S. *et al.* Study on the Landscape Space of Typical Mining Areas in Xuzhou City from 2000 to 2020 and Optimization Strategies for Carbon Sink Enhancement. *Remote Sensing* **14**, 4185 (2022).
36. Ma, Y. & Xu, Z. Construction of Low-Carbon Land Use and Management System in Coal Mining Areas. *Sustainability* **15**, 12486 (2023).
37. Fu, Y. *et al.* Dynamics of carbon storage driven by land use/land cover transformation in coal mining areas with a high groundwater table: A case study of Yanzhou Coal Mine, China. *Environmental Research* **247**, 118392 (2024).
38. Jiang, L., Liu, B. & Yuan, Y. Quantifying Vegetation Vulnerability to Climate Variability in China. *Remote Sensing* **14**, 3491 (2022).
39. Xin, D. *et al.* Research on top-level planning for sustainable high-quality development of China's largest scale deep coal mining area. *Frontiers in Earth Science* **11**, (2023).
40. Ding, Y. & Peng, S. Spatiotemporal Trends and Attribution of Drought across China from 1901–2100. *Sustainability* **12**, 477 (2020).
41. Peng, S., Ding, Y., Liu, W. & Li, Z. 1 km monthly temperature and precipitation dataset for China from 1901 to 2017. *Earth System Science Data* **11**, 1931–1946 (2019).
42. Yang, J. & Huang, X. The 30 m annual land cover dataset and its dynamics in China from 1990 to 2019. *Earth System Science Data* **13**, 3907–3925 (2021).
43. Pei, Z., Ouyang, H., Zhou, C. & Xu, X. Carbon Balance in an Alpine Steppe in the Qinghai-Tibet Plateau. *Journal of Integrative Plant Biology* **51**, 521–526 (2009).
44. Hurst, H. E. Long-Term Storage Capacity of Reservoirs. *Transactions of the American Society of Civil Engineers* https://doi.org/10.1016/0013-4694(51)90043-0 (1951) doi:10.1016/0013-4694(51)90043-0.
45. Wang, J. *et al.* Geographical Detectors-Based Health Risk Assessment and its Application in the Neural Tube Defects Study of the Heshun Region, China. *International Journal of*

Geographical Information Science **24**, 107–127 (2010).

46. Wang, J., Zhang, T. & Fu, B. A measure of spatial stratified heterogeneity. *Ecological Indicators* **67**, 250–256 (2016).
47. Fu, S., Bai, Z., Yang, B. & Xie, L. Study on ecological loss in coal mining area based on net primary productivity of vegetation. *Land* **11**, 1004 (2022).
48. Mao, R. *et al.* Evaluating net primary productivity dynamics and their response to land-use change in the loess plateau after the 'Grain for Green' program. *Journal of Environmental Management* **360**, (2024).
49. Chen, Y. *et al.* Spatial–Temporal Dynamics of Grassland Net Primary Productivity and Its Driving Mechanisms in Northern Shaanxi, China. *Agronomy* **13**, 2684 (2023).
50. Wei, H. *et al.* Ecosystem Services and Ecological Restoration in the Northern Shaanxi Loess Plateau, China, in Relation to Climate Fluctuation and Investments in Natural Capital. *Sustainability* **9**, 199 (2017).
51. Dai, L. *et al.* Analysis of Spatiotemporal Evolution Characteristics and Influencing Factors of Vegetation Net Primary Productivity in Shendong Mining Area. *Sustainability* **16**, 6564 (2024).
52. Ke, J. *et al.* Temporal and Spatial Variation of Vegetation in Net Primary Productivity of the Shendong Coal Mining Area, Inner Mongolia Autonomous Region. *Sustainability* **14**, (2022).
53. Jin, K., Wang, F., Yu, Q., Gou, J. & Liu, H. Varied degrees of urbanization effects on observed surface air temperature trends in China. *Climate Research* **76**, (2018).
54. Ye, W., van Dijk, A. I. J. M., Huete, A. & Yebra, M. Global trends in vegetation seasonality in the GIMMS NDVI3g and their robustness. *International Journal of Applied Earth Observation and Geoinformation* **94**, 102238 (2021).
55. Wu, X., Hao, W., Qu, G. & Yang, L. Spatial-Temporal Pattern of Vegetation Net Primary Productivity and Its Natural Driving Factors in Ordos Section of the Yellow River Basin. *Atmosphere* **16**, 89 (2025).
56. Chen, Y., Xu, Y., Chen, T., Zhang, F. & Zhu, S. Exploring the Spatiotemporal Dynamics and Driving Factors of Net Ecosystem Productivity in China from 1982 to 2020. *Remote Sensing* **16**, 60 (2024).